中国光学（中英文） Chinese Optics 核心期刊

Tunable reflective spin-decoupled encoding metasurface based on Dirac semimetals

ZHANG Hui-yun, HAO Xiao-yu, ZHENG Si-yu, WANG Yu, LIU Yang, LIU Meng, ZHANG Jin-juan, ZHANG Yuping

Citation:
ZHANG Hui-yun, HAO Xiao-yu, ZHENG Si-yu, WANG Yu, LIU Yang, LIU Meng, ZHANG Jin-juan, ZHANG Yuping. Tunable reflective spin-decoupled encoding metasurface based on Dirac semimetals[J]. *Chinese Optics*, In press. doi: 10.37188/CO.EN-2024-0037
, , , , , , , . ${article.titleCn}[J]. 中国光学, 优先发表. doi: 10.37188/CO.EN-2024-0037

View online: https://doi.org/10.37188/CO.EN-2024-0037

文章编号　2097-1842(xxxx)x-0001-10

Tunable reflective spin-decoupled encoding metasurface based on Dirac semimetals

ZHANG Hui-yun, HAO Xiao-yu, ZHENG Si-yu, WANG Yu, LIU Yang, LIU Meng, ZHANG Jin-juan*, ZHANG Yuping*

(*Qingdao Key Laboratory of Terahertz Technology*, *College of Electronic and Information Engineering*, *Shandong University of Science and Technology*, *Qingdao*, 266590, *China*)

* *Corresponding author*, *E-mail*: *zhangjinjuan@sdust.edu.cn*; *sdust_thz*@163.*com*

Abstract: Multiple functional metasurfaces with high information capacity have attracted considerable attention from researchers. This study proposes a 2-bit tunable decoupled coded metasurface designed for the terahertz band, which utilizes the tunable properties of Dirac semimetals (DSM) to create a novel multilayer structure. By incorporating both geometric and propagating phases into the metasurface design, we can effectively control the electromagnetic wave. When the Fermi energy level of the DSM is set at 6 meV, the electromagnetic wave is manipulated by the DSM patch to operate at a frequency of 1.3 THz. Conversely, at a Fermi energy level of 80 meV, the electromagnetic wave is similarly controlled to function at a frequency of 1.4 THz. Both modes enable independent control of beam splitting under left-rotating circularly polarized (LCP) and right-rotating circularly polarized (RCP) wave excitation, resulting in the generation of vortex beams with distinct orbital angular momentum (OAM) modes. The findings of this study hold significant potential for enhancing information capacity and polarization multiplexing techniques in wireless communications.

Key words: terahertz; dirac semimetal; spin decoupling; circular polarization; tunable

中图分类号:　**文献标志码:**A　**doi:**10.37188/CO.EN-2024-0037　**CSTR:**32171.14.CO.EN-2024-0037

1　Introduction

Metamaterials are a class of man-made composites characterized by unique physical properties, which are widely utilized for the control of electromagnetic waves. Metasurfaces, the two-dimensional counterparts of metamaterials, are distinguished by their small size, low loss, and straightforward manufacturing processes. They can effectively modulate the amplitude, phase, and polarization of electromagnetic wavefronts, enabling the realization of abnormal electromagnetic phenomena[1-2]. By designing the structural parameters and material properties of metasurfaces with arrays of meta-atoms, a variety of innovative devices in the field of electro-

收稿日期:xxxx-xx-xx; **修订日期:**xxxx-xx-xx

基金项目:中文基金

Supported by National Natural Science Foundation of China (No. 62375158, No. 62105187); Natural Science Foundation of Shandong Province (No. ZR2021QF010); Development Plan of Youth Innovation Team in Colleges and Universities of Shandong Province (No. 2022KJ216).

magnetic waves have been developed, including anomalous reflections[3-4], polarization conversion[5], radar cross-section (RCS) reduction[6], and vortex beams[7-9]. In 2014, Cui et al. introduced the concept of coded metasurfaces, which integrate coding with digital signals. For instance, a 1-bit coded metasurface consists of two discrete meta-atom units, each with phase responses of 0° and 180°, labeled as "0" and "1". These coding sequences are employed to achieve different functions. Furthermore, 2-bit and multi-bit coded metasurfaces can be realized, offering greater flexibility in the design of multifunctional metasurfaces[10-11]. Generally, meta-atoms regulate the phase response under varying incident wave irradiation through two pathways: the propagation phase and the geometric phase. The propagation phase can be controlled by adjusting the size of the meta-atom under linearly polarized incidence, while the anisotropic meta-atom operates in two orthogonally polarized states, x-polarized and y-polarized, to achieve the desired functionality[12]. In the context of geometrical phase, the meta-atom can achieve various orientation angles (α) to generate a specific phase shift (φ) under circularly polarized incidence through rotation. This relationship is expressed as $\varphi = \pm 2\alpha$, where the "+" and "−" symbols denote LCP and RCP incident waves, respectively[13-14]. However, the intrinsic characteristics of the geometrical phase cause the metasurface to produce completely antisymmetric responses under LCP and RCP incidences, which cannot be modulated independently. This limitation results in a lack of functional diversity in the metasurface concerning geometrical phase, highlighting the urgent need to achieve independent manipulation of circularly polarized waves.

Two distinct angular momentum modes are observed in photons: spin angular momentum (SAM), which is associated with the spin state of the electromagnetic wave, and orbital angular momentum (OAM), which pertains to the spatial phase of the electromagnetic wave[15-16]. The combination of geometrical and propagation phases can be employed to facilitate the conversion from SAM to OAM. The OAM carried by the vortex spin beam can significantly enhance the data capacity of communication systems, thereby providing new degrees of freedom that are crucial for multichannel optical and wireless communications. In 2018, Xu et al. proposed a strategy that integrates geometrical and propagation phases to overcome the intrinsic limitations of geometrical phases, thereby achieving the spin decoupling function. They designed two multifunctional circularly polarized bifunctional devices operating in the microwave region to validate their approach[15]. In 2019, Zhang et al. introduced an efficient transport metasurface with switchable functions for the independent manipulation of LCP and RCP waves. They realized switchable focused beams and the ability to switch between vortex beams and focused beams within the microwave region[17]. In 2022, Li et al. proposed a reflective spin-decoupled metasurface in the terahertz band that combines spin decoupling with the superposition theorem. Based on this concept, they successfully realized three types of metasurfaces: superpositions of multiple vortex beams and focusing beams, four-channel vortex beams, and four-channel focusing beams[18]. Given that the functionality of purely structured metasurfaces is constrained by fixed dimensions, dynamically tunable electromagnetic waves have garnered considerable attention from researchers. They aim to incorporate tunable materials such as graphene[19], indium antimonide[20], vanadium dioxide[21], and DSM[22] into metasurfaces, leading to the design of actively tunable metasurfaces with enhanced performance by varying external conditions such as temperature and voltage[23]. In 2021, Xu et al. proposed a graphene-based tunable metasurface capable of achieving two distinct functions: dynamic multibeam switching and dynamic diffusion switching, by modulating the Fermi energy level of graphene[24]. In 2023, Ma et al. introduced a vanadium dioxide-based coded metasurface

that facilitates the switching of vanadium dioxide between insulating and metallic states in response to temperature variations. This switching mechanism enables RCS scaling at different frequencies[25]. These tunable materials offer versatile dynamic tuning within a single metamaterial device. Notably, DSM, as a novel topological quantum material akin to 3D graphene, exhibit high carrier mobility and provide additional structural degrees of freedom for the construction of functional devices. Furthermore, DSM boasts stable performance, ease of preparation, and rapid response times. Consequently, integrating DSM into coded metasurfaces enhances the dynamic modulation of electromagnetic waves.

In this study, a multilayer structure based on a DSM is designed. By adjusting the size and rotation angle of the cross-shaped meta-atom, we intergrate propagation and geometric phases to create a 2-bit meta-atom library, which serves as the foundation for designing a tunable, spin-decoupled coded metasurface operating in the terahertz band. When the Fermi energy level of the DSM is set to 6 meV, the system operates at 1.3 THz. By varying the incidence modes of LCP and RCP waves, we achieve the switching of double vortex beams with topological charges $l = -2$ and $l = 1$. Similarly, when the Fermi energy level of the DSM is increased to 80 meV, the metasurface operates at 1.4 THz, again facilitating the switching of double vortex beams with the same topological charges. Consequently, the designed metasurface exhibits switchable characteristics, functioning effectively as a multichannel vortex beam generator.

2 Theory and method

To independently control the LCP waves and RCP waves, we introduce the concepts of geometric phase and propagation phase. Specifically, the reflected LCP and RCP waves are assigned additional phases, denoted as φ_L and φ_R[26]

$$\begin{aligned} \varphi_L &= \varphi_x - 2\alpha \\ \varphi_R &= \varphi_y - 2\alpha \end{aligned}, \tag{1}$$

Where α represents the cell rotation angle associated with the geometric phase, and φ_x and φ_y denote the reflected amplitude and phase of the *x*-polarized and *y*-polarized waves. The equation above can be reorganized to yield the following

$$\begin{aligned} \varphi_x &= (\varphi_R + \varphi_L)/2 \\ \varphi_y &= (\varphi_R + \varphi_L)/2 \\ \alpha &= (\varphi_R - \varphi_L)/4 \end{aligned}, \tag{2}$$

As there exists a reflection phase response characterized by a phase difference of π between the *x* and *y* polarizations (i.e., $\varphi_x - \varphi_y = \pi$), this indicates a distinct reflection phase for the *x* and *y* polarization incidences[18]

$$\begin{aligned} \varphi_x &= (\varphi_R + \varphi_L)/2 \\ \varphi_y &= (\varphi_R + \varphi_L)/2 - \pi \end{aligned}, \tag{3}$$

By the above equation, the two reflection phases, LCP and RCP, are independently controlled by designing the parameters φ_x, φ_y and α.

The structure of the designed meta-atom is illustrated in Fig. 1(a). The elements, arranged from top to bottom, consist of a cross-shaped DSM patch, a silica isolator with a dielectric constant of 3.85, a DSM film, a cross-shaped gold patch embedded within the DSM film, another silica isolator, and a gold substrate. The DSM patch, DSM film, and gold substrate each have a thickness of 0.5 μm, while the gold patch embedded in the DSM film has a thickness of 0.4 μm, and the silica isolator has a thickness of 20 μm. The cross structure aids in reducing crosstalk by minimizing variations between the polarized reflection phases φ_x and φ_y. Consequently, by adjusting the lengths of l_1 and l_2, as well as l_3 and l_4, it is possible to select an appropriate coding unit at two distinct Fermi energy levels. In this study, the simulation software CST Microwave Studio is employed for modeling, utilizing periodic boundary conditions in the x and y directions and open boundary conditions in the z direction. The complex conductivity of the DSM can be derived using Kubo's

formula within the framework of random phase approximation (RPA) theory. In the low temperature limit ($T<<E_F$), the dynamic conductivity of the DSM can be expressed as[27-28]

$$Re(\sigma(\Omega)) = \frac{e^2}{\hbar}\frac{gk_F}{24\pi}\Omega\theta(\Omega-2) \quad ,$$

$$Im(\sigma(\Omega)) = \frac{e^2}{\hbar}\frac{gk_F}{24\pi}\left[\frac{4}{\Omega} - ln\left(\frac{4\varepsilon_c}{|\Omega^2-4|}\right)\right] \quad ,$$

Where e is the electron charge, $\hbar$ is the approximate Planck constant, and $k_F = E_F/\hbar v_F$ is the Fermi momentum. $v_F = 10^6$ m/s is the Fermi velocity, E_F is the Fermi energy level, $\Omega = \hbar\omega/E_F + i\hbar\tau^{-1}/E_F$, where $\tau = \mu E_F/ev_F^2$ is the relaxation time, $\mu = 3\times 10^4$ cm^{2}V^{-1}s^{-1}, $\varepsilon_c = E_c/E_F$, and Ec is the cutoff energy. In this study, the AlCuFe quasicrystals that we have chosen as DSM, $g = 40$ is the simplex factor. The complex relative permittivity of the DSM can be expressed as:

$$\varepsilon = \varepsilon_b + i\sigma/\omega\varepsilon_0 \quad ,$$

Where $\varepsilon_b = 1$, ε_0 is the vacuum dielectric constant.

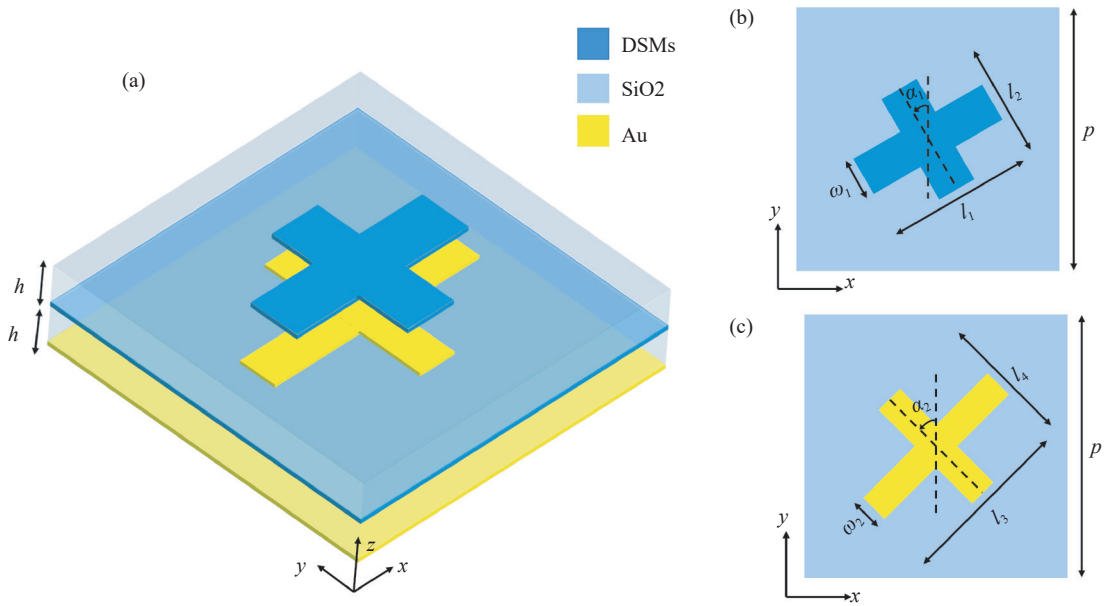

Fig. 1 (a) 3D schematic of the designed meta-atom. (b) Top view of the DSM patch in 2D. (c) Top view of the gold patch in 2D.

Fig. 1(b,c) present top views of the DSM patch and the gold patch, respectively. The period of the meta-atom is denoted as p = 100 μm, while the cross arm lengths of the DSM patch and the gold patch are represented as l_1, l_2, l_3, and l_4. The widths are defined as ω_1 = 15 μm and ω_2 = 11 μm. By adjusting the cross arm lengths l_1, l_2, l_3, and l_4, we can control the propagation phase, while the rotation angles α_1 and α_2 allow for the control of the geometric phase. Consequently, the design of our desired meta-atom, which meets the conditions for both the propagation phase and geometric phase, is achieved through the variation of the aforementioned parameters.

To obtain ideal meta-atoms, the amplitude and phase responses of meta-atoms at various DSM Fermi energy levels are investigated. The simulation software CST Microwave Studio is employed to model the designed meta-atoms, applying periodic boundary conditions in the x and y directions and open boundary conditions in the z direction. At a DSM Fermi energy level of E_F = 6 meV, the phase response is modulated by the gold patch. Consequently, the design of the gold patch parameters is streamlined, as there is no need to consider additional specific parameters or variations in the rotation

angle of the DSM patch. Low crosstalk between *x*- and *y*-linear polarization is observed due to the cross structure; when the rotation angle α_2 in Fig. 1(c) is set to 0°, the parameters l_3 and l_4 determine the reflection phase response for *x*-polarization and *y*-polarization, respectively. With parameter l_4 fixed between 15 μm and 95 μm and α_2 held at 0°, varying parameter l_3 adjusts the reflected phase of the x-polarized waves, while the reflection amplitude and phase for y-polarization remain largely unaffected by changes in parameter l_3. Fig. 2(a) demonstrates that simulations of meta-atoms at a DSM Fermi energy level of 6 meV yield amplitude and phase results obtained by varying parameter l_3 of the gold patch. The eight values of parameter l_3 are 67.5 μm, 61.5 μm, 56.9 μm, 53.2 μm, 52.8 μm, 49.2 μm, 42.5 μm, and 15 μm, denoted by the numbers 1 to 8. As illustrated in the figure, the reflection amplitudes of the meta-atoms exceed 0.6 at 1.3 THz, with reflection phases varying from 0° to 360°. Fig. 2(b) shows that eight coding units with a phase difference of approximately 180° between φ_{xx} and φ_{yy} were identified by adjusting the cross arm length at 1.3 THz, satisfying the requirement for 360° phase coverage in both *x*-polarization and *y*-polarization.

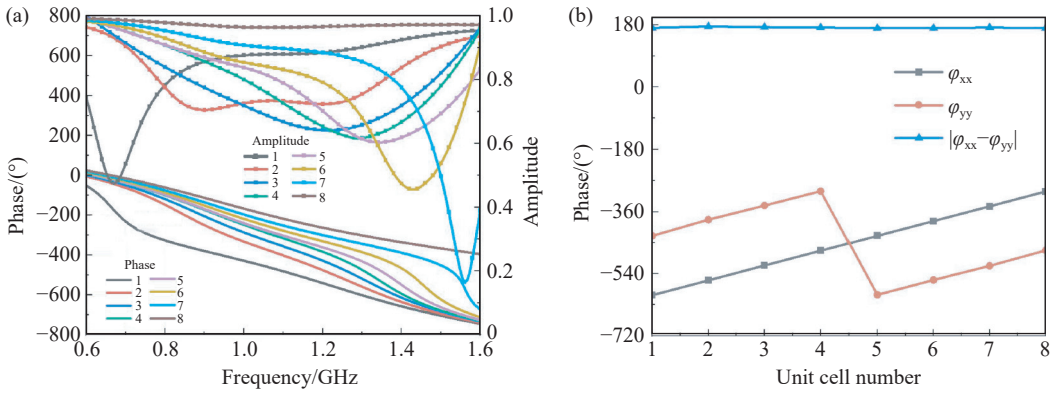

Fig. 2 When E_F = 6 meV (a) simulated reflectance spectral amplitude and phase of 8 cell parameters of gold patches at x-polarized incidence. (b) 8 meta-atoms covering a 2π phase range at 45°intervals under linearly polarized wave incidence.

The objective of the meta-atom design is to facilitate the generation of two independent coding states for LCP and RCP light. It is evident from the previous derivation in Eq.(3) that RCP/LCP wave incidence must achieve 360° phase coverage to meet the phase requirement. The phases φ_{LCP} and φ_{RCP} are discretized into 0°, 90°, 180°, and 270° within a 2-bit code, corresponding to propagation phases of 0°, 45°, 90°, and 135°, respectively. By rotating eight meta-atoms at 22.5° intervals and combining the four states of LCP and RCP, we can create a library of 16 meta-atoms, As shown in Fig. 3.

Similar to Fig.2, Fig.4 presents the simulation results of the meta-atom at 1.4 THz, specifically at the DSM Fermi energy level E_F=80meV, during which the DSM exerts a dominant influence over the electromagnetic wave. When the rotation angle α_1, as shown in Fig.1(b), is fixed at 0°, the parameters l_1 and l_2 dictate the reflection phase response for x and y polarization, respectively. With the parameter l_2 fixed at one of the values ranging from 11 μm to 95 μm and α_1 set at 0°, varying the parameter l_1 allows for the control of the phase of the reflection of *x*-polarized waves. Fig. 4(a) illustrates that simulations of meta-atoms at a DSM Fermi energy level of 80 meV yield amplitudes and phases that are obtained by varying the gold patch parameter l_1. The eight values of the parameter l_1 are 80 μm, 56.4 μm, 52 μm, 46.3 μm, 46 μm, 43 μm, 38.8 μm, and 17 μm, corresponding to the integers from 1 to 8. As illustrated in the Fig. 4(a), the amplitude phase of the coding unit exhibits significant changes under *x*-po-

larization when compared to 6 meV. The reflection amplitudes of the meta-atoms consistently exceed 0.6 at 1.4 THz, with the reflection phases varying correspondingly within the range of 0° to 360°. Fig. 4(b) demonstrates that at 1.4 THz, by adjusting the cross arm lengths, eight coding units were identified with a phase difference of approximately 180° between φ_{xx} and φ_{yy}. These eight coding units achieve 360° phase coverage in both *x*-polarization and *y*-polarization.

Utilizing the previously mentioned method, the four LCP and RCP states are combined to create an additional library of 16 meta-atoms., As shown in Fig. 5.

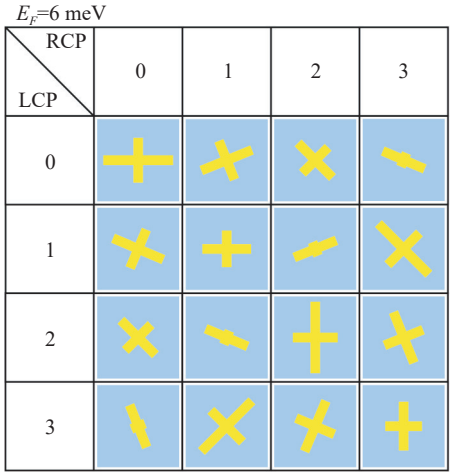

Fig. 3 Selected 16 meta-atoms in a 2-bit phase-modulated gold patch structure in *x*-polarization and *y*-polarization.

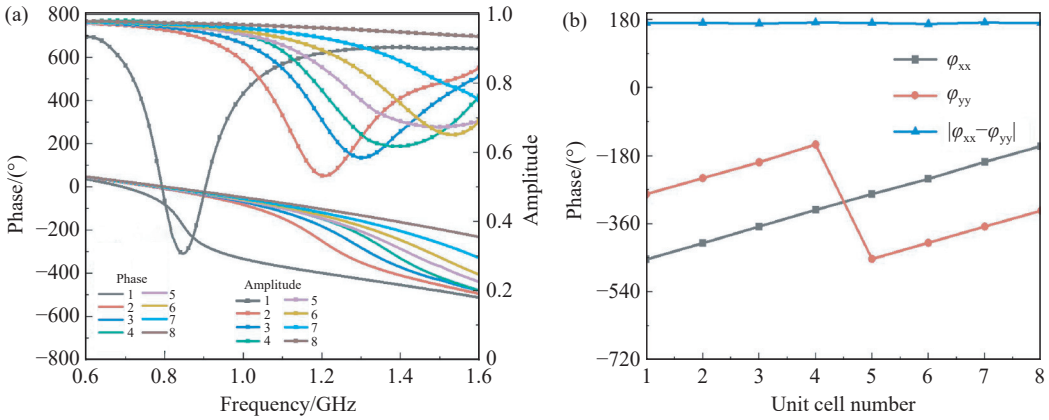

Fig. 4 When E_F = 80 meV (a) Simulated reflectance spectral amplitude and phase of 8 cell parameters of DSMs patch at *x*-polarized incidence. (b) 8 metaparticles covering a 2π phase range at 45°intervals under linearly polarized wave incidence.

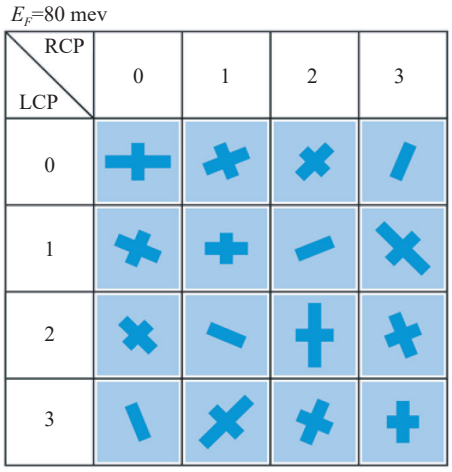

Fig. 5 Selected 16 meta-atoms in the 2-bit phase-modulated DSMs patch structure in *x*-polarization and *y*-polarization.

3 Results and discussion

The vortex beam enhances communication system performance by improving traffic volume and rate, while also facilitating multi-channel communications. To assess the feasibility of the model and elaborate on the design flow, several coded metasurfaces for generating helical OAM are demonstrated alongside their corresponding simulation results. The phase distribution of the vortex beam generator must conform to a spiral phase distribution, represented as $\varphi(x,y) = l\varphi = larctan(y/x)$, where l denotes the topological charge of the vortex beam, φ is the

azimuthal angle along the propagation direction[29-30], and x and y represent the horizontal and vertical coordinates of the center of any meta-atom, respectively. For a 2-bit coded metasurface, the phase difference between neighboring coded areas is 90°. When the E_F is set to 6 meV for the DSM, Fig. 6(c) illustrates the topological charge $l = -2$ convolved with the coding sequence of the periodic pattern "0000222200002222" along the y-direction for the LCP wave design. Similarly, Fig. 6(g) displays the convolution of $l = 1$ with the coded sequence of the same periodic pattern along the x-direction for the RCP wave design. Meta-atoms with suitable phase responses are selected from the library established in Fig. 3 to model the corresponding coding patterns. The designed coded metasurface comprises 16×16 cells, and simulations of the metasurface were conducted using CST Microwave Studio, applying open spatial boundary conditions in the x, y, and z directions. 3D normalized far-field scattering maps for the incidence of LCP and RCP waves are presented in Fig. 6(d,h). The vortex beam splitting with topological charge l = -2 occurred under LCP wave incidence, while the vortex beam splitting with topological charge l = 1 was observed under RCP wave incidence. This result indicates that it is possible to independently manipulate LCP or RCP waves by utilizing a pre-designed reflection-encoded metasurface, enabling the generation of distinct independent OAM modes for different circular polarization wave incidences. Fig. 6(i,j) illustrate the corresponding 2D far-field scattering maps for the incidence of LCP and RCP waves, while Fig. 6(k,l) present the corresponding vortex phases. From these figures, it is evident that the reflected beams achieve phase coverage of 720° and 360°, respectively, which aligns with the topological charges l = -2 and l = 1 associated with the OAM.

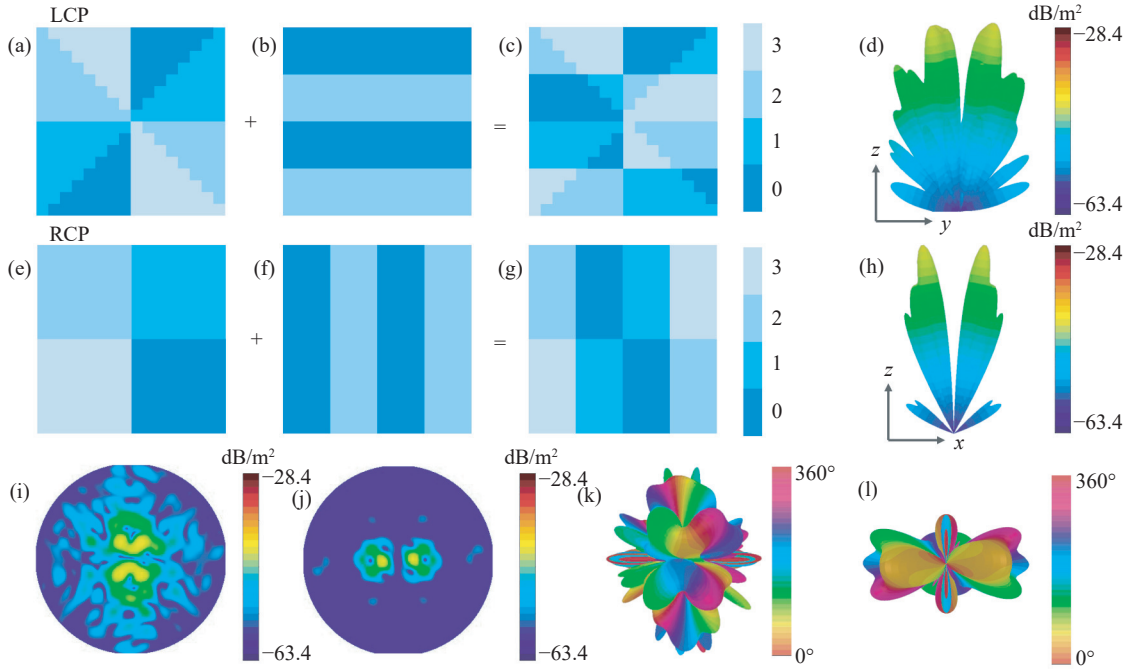

Fig. 6 When E_F = 6 meV (a, e) Vortex phase distributions for l = −2 with l = 1. (b, f) Phase distribution of gradients varying along the y-axis as well as the x-axis. (c, g) reflection coding map under LCP wave and RCP wave incidence. (d, h) 3D far-field map under LCP wave and RCP wave incidence. (i, j) 2D maps under the incidence of LCP wave and RCP wave. (k, l) vortex phases under incidence of LCP wave and RCP wave.

When the E_F is set to 80 meV in the DSM, Fig. 7(a) illustrates the convolution of the topological charge l = −1 with the coding sequence of the periodic pattern "0000222200002222" along the y-direction for the RCP wave design. Conversely, Fig. 7(e) depicts the LCP wave design for l = 0,

where the coding sequence along the x-direction is also "0000222200002222". Appropriate meta-atoms with the necessary phase response are selected from the library presented in Fig. 4 to model the corresponding coding patterns. The designed coded metasurface comprises 16×16 cells. The simulation of the metasurface was performed using the commercial software CST Microwave Studio, applying open and spatial boundary conditions in the x, y, and z directions. The 3D normalized far-field scattering maps for the incidence of LCP and RCP waves are presented in Fig. 7(d,h). At LCP wave incidence, a splitting of the vortex beam with topological charge $l = -1$ occurs, while a similar splitting is observed for the RCP wave incidence. Figs. 7(b,f) depict the corresponding 2D far-field scattering maps for LCP and RCP waves, respectively, while Figs. 7(c,g) illustrate the associated vortex phases. Notably, Fig. 7(d) indicates that the reflected beam exhibits a 360° phase coverage, which aligns with the topological charge $l = -1$ of the OAM.

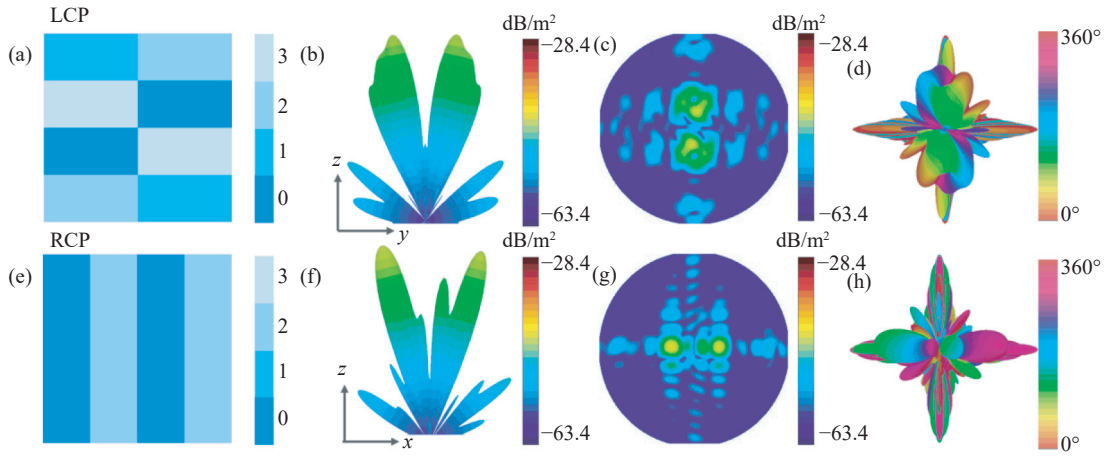

Fig. 7 When E_F = 80 meV (a, e) reflection coding map under LCP wave and RCP wave incidence. (b, f) 3D far-field map under LCP wave and RCP wave incidence. (c, g) 2D maps under the incidence of LCP wave and RCP wave. (d, h) vortex phases under incidence of LCP wave and RCP wave.

4 Conclusions

In summary, this paper presents a multi-functional metasurface. The switching of terahertz waveband functions is achieved by incorporating geometrical and propagation phases within the metasurface structure. At a Fermi energy level of 6 meV for DSM, the gold patch effectively controls the electromagnetic wave, generating vortex beam splitting with a topological charge of $l = -2$ for the LCP wave, and vortex beam splitting with a topological charge of $l = 1$ for the RCP wave. At a Fermi energy level of 80 meV for DSM, the DSM exerts complete control over electromagnetic waves, resulting in vortex beam splitting with a topological charge of $l = 1$ for the LCP wave, and beam splitting for the RCP wave. The findings of this study hold promising applications in the field of terahertz communication.

CRediT authorship contribution statement

Huiyun Zhang: Writing–review & editing, Supervision. **Xiaoyu Hao:** Writing–original draft, Software, Investigation, Conceptualization. **Siyu Zheng:** Visualization, Validation. **Yu Wang:** Software, Data curation. **Yang Liu:**Software. **Meng Liu:**Supervision, Resources. Jinjuan Zhang: Supervision, Resources.**Yuping Zhang:**Supervision, Resources.

Declaration of competing interest

The authors declare that they have no known

competing financial interests or personal relationships that could have appeared to influence the work reported in this paper.

Data availability

Data will be made available on request.

References:

[1] WANG M T, LIAO D SH, DAI J Y, *et al*.. Dual-polarized reconfigurable metasurface for multifunctional control of electromagnetic waves[J]. *IEEE Transactions on Antennas and Propagation*, 2022, 70(6): 4539-4548.

[2] LUO X G. Principles of electromagnetic waves in metasurfaces[J]. *Science China Physics*, *Mechanics & Astronomy*, 2015, 58(9): 594201, doi: 10.1007/s11433-015-5688-1.

[3] HUANG CH, PAN W B, MA X L, *et al*.. Multi-spectral metasurface for different functional control of reflection waves[J]. *Scientific Reports*, 2016, 6: 23291.

[4] LI L L, CUI T J, JI W, *et al*.. Electromagnetic reprogrammable coding-metasurface holograms[J]. *Nature Communications*, 2017, 8(1): 197.

[5] LI ZH Y, LI S J, HAN B W, *et al*.. Quad-band transmissive metasurface with linear to dual-circular polarization conversion simultaneously[J]. *Advanced Theory and Simulations*, 2021, 4(8): 2100117.

[6] XING W T, SI L M, DONG L, *et al*.. Rapid design of hybrid mechanism metasurface with random coding for terahertz dual-band RCS reduction[J]. *Optics Express*, 2023, 31(17): 28444-28458.

[7] YUAN Y Y, ZHANG K, RATNI B, *et al*.. Independent phase modulation for quadruplex polarization channels enabled by chirality-assisted geometric-phase metasurfaces[J]. *Nature Communications*, 2020, 11(1): 4186.

[8] LI S J, LI ZH Y, HUANG G SH, *et al*.. Digital coding transmissive metasurface for multi-OAM-beam[J]. *Frontiers of Physics*, 2022, 17(6): 62501.

[9] CHEN P, MA L L, HU W, *et al*.. Chirality invertible superstructure mediated active planar optics[J]. *Nature Communications*, 2019, 10(1): 2518.

[10] CUI T J, QI M Q, WAN X, *et al*.. Coding metamaterials, digital metamaterials and programmable metamaterials[J]. *Light*: *Science & Applications*, 2014, 3(10): e218, doi: 10.1038/lsa.2014.99.

[11] ZHANG ZH X, GAO L. 2-bit coding metasurface with a double layer random flip structure for wide band diffuse reflection and reciprocity protected transmission[J]. *Optics Express*, 2023, 31(20): 32253-32262.

[12] LIU SH, CUI T J, XU Q, *et al*.. Anisotropic coding metamaterials and their powerful manipulation of differently polarized terahertz waves[J]. *Light*: *Science & Applications*, 2016, 5(5): e16076, doi: 10.1038/lsa.2016.76.

[13] ZHANG L, LIU SH, LI L L, *et al*.. Spin-controlled multiple pencil beams and vortex beams with different polarizations generated by pancharatnam-berry coding metasurfaces[J]. *ACS Applied Materials & Interfaces*, 2017, 9(41): 36447-36455.

[14] CHENG G, SI L M, SHEN Q T, *et al*.. Transmissive Pancharatnam-Berry metasurfaces with stable amplitude and precise phase modulations using dartboard discretization configuration[J]. *Optics Express*, 2023, 31(19): 30815-30831.

[15] CHONG A, WAN CH H, CHEN J, *et al*.. Generation of spatiotemporal optical vortices with controllable transverse orbital angular momentum[J]. *Nature Photonics*, 2020, 14(6): 350-354.

[16] GUO Y H, ZHANG SH C, PU M B, *et al*.. Spin-decoupled metasurface for simultaneous detection of spin and orbital angular momenta via momentum transformation[J]. *Light*: *Science & Applications*, 2021, 10(1): 63, doi: 10.1038/s41377-021-00497-7.

[17] ZHANG K, YUAN Y Y, DING X M, *et al*.. High-efficiency metalenses with switchable functionalities in microwave region[J]. *ACS Applied Materials & Interfaces*, 2019, 11(31): 28423-28430.

[18] LI J SH, CHEN J ZH. Simultaneous and independent regulation of circularly polarized terahertz wave based on metasurface[J]. *Optics Express*, 2022, 30(12): 20298-20310.

[19] WANG F, ZHANG Y B, TIAN CH SH, *et al*.. Gate-variable optical transitions in graphene[J]. *Science*, 2008, 320(5873): 206-209.

[20] IYER P P, PENDHARKAR M, SCHULLER J A. Electrically reconfigurable metasurfaces using heterojunction resonators[J]. *Advanced Optical Materials*, 2016, 4(10): 1582-1588.

[21] DU ZH Q, HE C H, XIN J H, *et al*.. Terahertz dynamic multichannel holograms generated by spin-multiplexing

reflective metasurface[J]. *Optics Express*, 2024, 32(1): 248-259.

[22] ZHANG Y P, JIANG CH Y, LI ZH K, *et al*.. Circularly polarized terahertz wave independently controlled tunable spin-decoupled metasurface[J]. *Results in Physics*, 2024, 56: 107287.

[23] CUI T J, LI L L, LIU SH, *et al*.. Information metamaterial systems[J]. *iScience*, 2020, 23(8): 101403.

[24] XU J SH, LIU W W, SONG ZH Y. Terahertz dynamic beam steering based on graphene coding metasurfaces[J]. *IEEE Photonics Journal*, 2021, 13(4): 4600409.

[25] MA H R, YANG J J, CHEN T T, *et al*.. Tunable metasurface for independent controlling radar stealth properties via geometric and propagation phase modulation[J]. *Optics Express*, 2023, 31(7): 11760-11774.

[26] DING G W, CHEN K, LUO X Y, *et al*.. Dual-helicity decoupled coding metasurface for independent spin-to-orbital angular momentum conversion[J]. *Physical Review Applied*, 2019, 11(4): 044043.

[27] KOTOV O V, LOZOVIK Y E. Dielectric response and novel electromagnetic modes in three-dimensional Dirac semimetal films[J]. *Physical Review B*, 2016, 93(23): 235417.

[28] JIANG CH Y, LI ZH K, LV X Y, *et al*.. Active modulation of terahertz vortex beams by Dirac semimetals-based space-time-coding metasurface[J]. *Optics Communications*, 2023, 540: 129506.

[29] XIN J H, DU ZH Q, ZHOU Z K, *et al*.. Optical reflective metasurfaces enable spin-decoupled OAM and focusing[J]. *Physical Chemistry Chemical Physics*, 2023, 25(40): 27008-27016.

[30] HE C H, PAN Z M, SONG ZH Y. Manipulating spin-dependent wavefronts of vortex beams via plasmonic metasurfaces[J]. *Annalen der Physik*, 2023, 535(10): 2300235.